

Accelerating Bubble Detachment in Porous Transport Layers with Patterned Through-Pores

Jason K. Lee, ChungHyuk Lee, Kieran F. Fahy, Pascal J. Kim, Kevin Krause, Jacob M. LaManna, Elias Baltic, David L. Jacobson, Daniel S. Hussey, and Aimy Bazylak*



Cite This: <https://dx.doi.org/10.1021/acsaem.0c01239>



Read Online

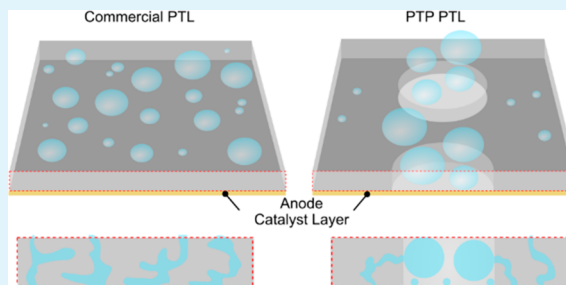
ACCESS |

Metrics & More

Article Recommendations

ABSTRACT: Mass transport losses ultimately suppress gas evolving electrochemical energy conversion technologies, such as fuel cells and carbon dioxide electrolyzers, from reaching the high current densities needed to realize commercial success. In this work, we reach ultrahigh current densities up to 9 A/cm² in a polymer electrolyte membrane (PEM) water electrolyzer with the application of custom porous transport layers (PTLs) with patterned through-pores (PTPs), and we reduce the mass transport overpotentials of the electrolyzer by up to 76.7%. This dramatic performance improvement stems from the 43.5% reduction in gas saturation at the catalyst layer-PTL interface region. Moreover, the presence of PTPs leads to more rapid bubble coalescence and subsequently more frequent bubble snap-off (~3.3 Hz), thereby enhancing the rate of gas removal and liquid water reactant delivery to the reaction sites. This work is highly informative for designing PTLs for optimal gas removal for a wide range of gas evolving electrochemical energy conversion technologies.

KEYWORDS: polymer electrolyte membrane electrolyzer, water electrolysis, hydrogen, porous transport layer, neutron radiography, synchrotron X-ray, in-operando imaging, two-phase flow



INTRODUCTION

The intermittency of renewable energy sources, such as the sun and wind, introduces prohibitive complexity and efficiency losses for grid integration. However, renewable energy can be stored as hydrogen and used with fuel cells to overcome this intermittency for clean, on-demand power. The polymer electrolyte membrane (PEM) water electrolyzer is a promising electrochemical energy conversion device for hydrogen production;^{1–3} however, PEM electrolyzers have not experienced widespread commercialization mainly due to their high capital expenditures (capex) and operational expenditures (opex).^{4–6} In particular, the stack cost contributes 53%–60% of the total electrolyzer plant cost,⁷ where the cost of end plates and flow field plates constitute 48% to 51% of the total cost of an electrolyzer stack,^{4,8,9} owing particularly to the titanium materials needed to withstand the corrosive environment at the anode. A strategic means for reducing the capex of a PEM electrolyzer stack is to operate at high current density conditions, thereby reducing the number of required cells in a stack to produce the same amount of hydrogen.⁵ Moreover, the optimal current density for minimal opex and capex has been reported to be $i = 2.5$ A/cm², but the optimal current density is expected to increase to $i = 10$ A/cm² in the near future with the decreasing cost of electricity.¹⁰ However, mass transport losses must first be minimized in order to facilitate

high current density operation. While extensive research has been conducted for designing the catalyst layer^{11–13} and membrane¹⁴ to advance electrolyzer performance, the strategic design of porous transport layers (PTLs) for high current density operation ($i > 5$ A/cm²) has been largely overlooked in the field.

The anode PTL must facilitate reactant (water) transport and by-product (oxygen) removal. Liquid water is delivered from the anode flow channels to the reaction sites through pores in the anode PTL. When current is applied, the oxygen evolution reaction initiates at the reaction sites and generates protons, electrons, and oxygen molecules. As the reaction progresses, byproduct oxygen molecules nucleate as gas bubbles at the reaction sites and accumulate inside the pores of the PTL. The resulting pore blockage impedes liquid water reactant transport to the reaction sites and leads to undesirable mass transport losses. Suermann et al.¹⁵ demonstrate that mass transport losses contribute up to 25% of the total losses in an

Received: May 29, 2020

Accepted: September 9, 2020

Published: September 9, 2020

electrolyzer cell at current densities below $i < 5 \text{ A/cm}^2$. For PEM water electrolyzers, mass transport losses are identified using electrochemical techniques, including electrochemical impedance spectroscopy (EIS),^{16–21} polarization curves,^{7,22,23} and Tafel approximations.^{15,24–29} The low frequency impedance measured from the EIS is typically associated with mass transport losses in PEM electrolyzers.^{16–21} Polarization curves also indicate mass transport losses in PEM electrolyzers. Specifically, a sudden increase in the cell potential at high current density is indicative of mass transport losses.^{7,22,23} A frequently used method in the literature for estimating mass transport overpotential is via calculating the kinetic overpotential with the Tafel slope and solving for mass transport losses.^{15,24–29} Although the estimated mass transport loss calculated using the Tafel approximation includes both contributions of mass transport losses from proton transport and mass transport,²⁴ it still provides useful information when investigating mass transport behavior in PEM electrolyzers. Electrochemical analyses are powerful for understanding how PTL materials can be tailored to improve the performance of PEM electrolyzers.

The PTL structure can be tuned to enhance mass transport behavior in PEM electrolyzers.^{17,18,30–38} Grigoriev et al.³⁰ evaluate the electrochemical performance of PEM electrolyzers with that of various types of sintered titanium powder-based PTLs and suggest that average pore sizes greater than $11 \mu\text{m}$ result in minimized mass transport losses. Lettenmeier et al.³¹ use plasma spraying to fabricate custom PTLs with a backing layer, which leads to a 5 % improvement in PEM electrolyzer efficiency compared to a commercial PTL. Kang et al. report a novel PTL structure featuring thin-tunable through-pores and demonstrate superior cell performance compared to commercial PTL materials.^{33,34} The mass transport within the PTLs heavily rely on the through-pores for the supply of liquid water and the removal of gas in the electrolyzer cell. However, the through-pore PTLs are designed with inactive pores under the lands that can lead to inefficient water transport in the in-plane direction.³⁹ These through-pore PTL studies strongly illustrate the importance of in-plane liquid water transport for enhancing mass transport behavior.

Two types of electrolyzer stacks are found in the literature: electrolyzers with conventional flow fields and those without the flow fields. While flow channels promote effective two-phase transport in the electrolyzer,^{41–44} their high manufacturing costs make electrolyzer designs without flow fields an attractive alternative.^{45,46} Previous studies in the literature report that electrolyzers without flow fields are more susceptible to mass transport losses.^{17,22,47} Specifically, Lickert et al.²² examine multiple PTLs at high current densities (up to 5 A/cm^2) and conclude that the anode PTL design is key for improving the performance of PEM electrolyzers.

The water/oxygen mass transport characteristics of PTLs can be analyzed via direct in operando visualization techniques.^{48–53} For instance, Hoeh et al. use in operando synchrotron X-ray imaging to observe the gas bubble growth and detachment at the PTL-flow field interface,⁴⁸ and Leonard et al.⁴⁹ use synchrotron X-ray imaging to quantify bubble residence time in a PEM electrolyzer. Lee et al.⁵⁰ use a combination of in operando neutron imaging and computational fluid dynamics modeling to demonstrate and explain the benefits of higher operating temperatures to the mass transport behavior in PEM electrolyzers.

In this work, we propose a new PTL design with enhanced mass transport properties, and we fully characterize the mass transport behavior with in operando neutron and X-ray imaging. We modify a commercial sintered titanium powder-based PTL by adding patterned through-pores (PTPs) under the channel regions to facilitate effective gas removal while preserving regular pores in a commercial PTL for liquid water permeation to the reaction sites. We characterize the steady-state gas saturation inside the PTP PTL via in operando neutron imaging in the in-plane direction (beam axis parallel to the membrane), and we characterize the dynamic gas transport behavior at the PTL-flow field interface via subsecond in operando synchrotron X-ray imaging in the through-plane direction (beam axis perpendicular to the membrane).

EXPERIMENTAL METHODS

In this section, we describe our custom PTP PTL and the method by which we examine the in operando electrochemical performance. Next, we describe our approach for concurrent electrochemical performance characterization with in operando imaging via both neutron and synchrotron X-ray imaging.

Electrolyzer Cell and the PTP PTL. Our electrolyzer cell design is customized for in operando visualization experiments. The electrolyzer cell consists of a small $5 \text{ mm} \times 16 \text{ mm}$ active area, which is specifically sized to maximize the contrast between water and gas in the PTL via neutron imaging. Grade-II titanium flow field plates have 16 parallel channels for both anode and cathode compartments and are plated with a $0.5 \mu\text{m}$ thick layer of gold and a $2.5 \mu\text{m}$ thick layer of platinum to ensure stability in the corrosive environment of the PEM electrolyzer anode. A commercially available sintered titanium powder-based PTL (1100 series, Mott Corp.¹) is used as the base material for the custom anode PTL featuring patterned through-pores. For the cathode PTL, the pristine 1100 series commercial PTL is used (without any modifications). Both anode and cathode PTLs are compressed during cell assembly by using $250 \mu\text{m}$ thick rigid polytetrafluoroethylene gaskets. We use a commercially available thin catalyst coated membrane to operate at high current densities. Specifically, we use Nafion HP membranes coated with 1.0 mg/cm^2 iridium (anode compartment) and 0.3 mg/cm^2 platinum (cathode compartment) (HYDRion HP, Ion Power). For comparison, the in operando visualization experiments are repeated using the identical electrolyzer setup using the pristine commercial PTL as the anode PTL.

The PTP PTL used as the anode PTL is fabricated by machining PTPs in a commercial sintered titanium powder-based PTL. Specifically, through-pores are created by perforating the commercial PTL to promote both effective gas removal (via through-pores) and reactant liquid water transport (via regular pores in the PTL) during electrolysis. As seen from Figure 1, the PTL region under each channel consists of three through-pores equally spaced along the length of the channel. Each through-pore has a diameter of $400 \mu\text{m}$ for a total of 48 through-pores across the entire active area (16 channels with 3 through-pores per channel). The center-to-center distance between each through-pore is $1000 \mu\text{m}$ across the channel and $2000 \mu\text{m}$ along the channel. In our previous study,^{39,40} we found that through-pores placed under the channels are more effective than those placed under the land for facilitating effective mass transport in PEM electrolyzers. Therefore, here, we strategically place PTPs only under the channel regions to minimize losses associated with reduced electrical contact area and electrochemical surface area.

Electrochemical Performance Analysis. All presented electrochemical results are acquired in operando with neutron imaging using the electrolyzer with an active area of $5 \text{ mm} \times 16 \text{ mm}$. We maintain the electrolyzer cell temperature at $75 \text{ }^\circ\text{C}$ while flowing deionized liquid water at a rate of 1.5 mL/min through both the anode and cathode compartments. A circulating heated bath (Isotemp heated bath circulator, Fisher Scientific) is connected to the electrolyzer cell to control the cell temperature. An in-line peristaltic pump

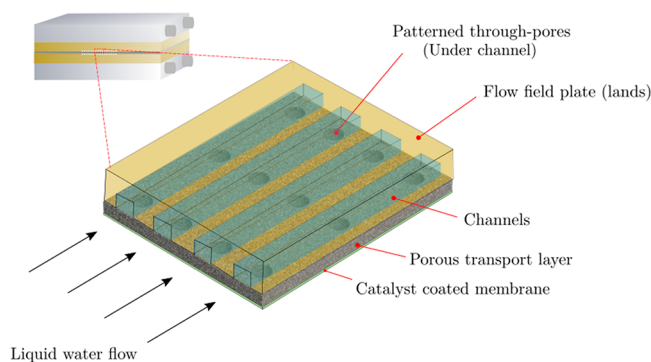


Figure 1. A schematic of the PTP PTL. Patterned through-pores ($d = 400 \mu\text{m}$) are machined under the channel region to improve mass transport in a PEM electrolyzer. There are three through-pores along the length of each channel with 16 channels in total.

(Masterflex L/S precision variable speed console drive, Cole-Parmer) with a pulse dampener is used to ensure a constant reactant flow rate of 1.5 mL/min to both anode and cathode compartments. The electrolyzer cell operates at atmospheric pressure.

We first perform galvanostatic polarization concurrently with neutron imaging to correlate the electrolyzer cell performance to steady state mass transport behavior. By operating under galvanostatic mode, we maintain a constant reaction rate in the anode compartment regardless of the PTL type used in the electrolyzer cell. We focus on high current density operations to observe mass transport behavior within PTP and commercial PTLs. A potentiostat (Reference 3000, Gamry Instruments) with an add-on booster (Reference 30k Booster, Gamry Instruments) is used to acquire polarization curves. Each constant current density operation is held for 15 min at $i = 1 \text{ A/cm}^2$, 3 A/cm^2 , 5 A/cm^2 , 7 A/cm^2 , and 9 A/cm^2 , and we report values averaged over the last 5 min to capture steady-state operation (deviation of the cell potential $< 5\%$).

While EIS is an excellent technique for characterizing mass transport losses, we use the Tafel approximation in this work to correlate mass transport overpotential with PTL gas saturation because applying current perturbations to the electrolyzer will impact the gas saturation measurements at each current density during in operando neutron imaging. Hence, the Tafel slope is measured at $i = 60 \text{ mA/cm}^2$ to 160 mA/cm^2 (with a 20 s hold for each current step) twice, and the average is taken to approximate the mass transport overpotential for each PTL. The Tafel approximation has been widely used in the literature for PEM water electrolyzers to approximate the contribution of mass transport losses.^{15,24–29} It is important to acknowledge that the mass transport overpotential calculated using the Tafel approximation method, presented in this work, consists of both contributions from interfacial resistance (proton resistance)^{24,25,28} and gas accumulation in the anode PTL.⁵⁴ The mass transport overpotential calculated from Tafel approximation is used as an indicator to compare the mass transport properties of the PTP PTL and commercial PTL at high current densities. The following relation is used to approximate the mass transport overpotential

$$E_{\text{cell}} = E_{\text{rev}} + \eta_{\text{ohmic}} + \eta_{\text{kinetic}} + \eta_{\text{mass transport}} \quad (1)$$

where E_{cell} is the measured cell potential [V], E_{rev} is the reversible potential [V], η_{ohmic} is the ohmic overpotential [V], η_{kinetic} is the kinetic overpotential [V], and $\eta_{\text{mass transport}}$ is the mass transport overpotential [V]. We apply an empirical correlation demonstrated by LeRoy et al. to calculate the reversible potential⁵⁵

$$E_{\text{rev}} = 1.5184 - 1.5421 \times 10^{-3} \cdot T + 9.523 \times 10^{-5} \cdot T \cdot \ln T + 9.84 \times 10^{-8} \cdot T^2 \quad (2)$$

The ohmic overpotential is calculated using the high frequency resistance (HFR, R_{ohmic}) measured with the current interrupt method

$$\eta_{\text{ohmic}} = i \cdot R_{\text{ohmic}} \quad (3)$$

where i is the current density [A/cm^2]. The HFR measurements are obtained after each tested constant current density to accurately represent the ohmic contribution to the total overpotential. The following equation is used to approximate the kinetic overpotential

$$\eta_{\text{kinetic}} = b \cdot \log_{10} \left(\frac{i}{i_0} \right) \quad (4)$$

where b represents the measured Tafel slope [V/dec] from each electrolyzer cell, and i_0 represents the apparent exchange current density [A/cm^2]. The mass transport overpotentials for each electrolyzer cell with the PTP and commercial PTLs are approximated by solving for $\eta_{\text{mass transport}}$ in eq 1 with all other variables determined.

Neutron Radiography for Quantifying Gas Saturation. In operando neutron imaging is used to quantify steady state gas saturation in both the PTP and commercial PTLs in the in-plane direction (i.e., beam axis parallel to the membrane). The experiments are performed at the Neutron Imaging Facility (BT-2) located in the National Institute of Standards and Technology (NIST) Center for Neutron Research (Gaithersburg, MD).⁵⁶ The setup of the electrolyzers is as shown in Figure 2a.

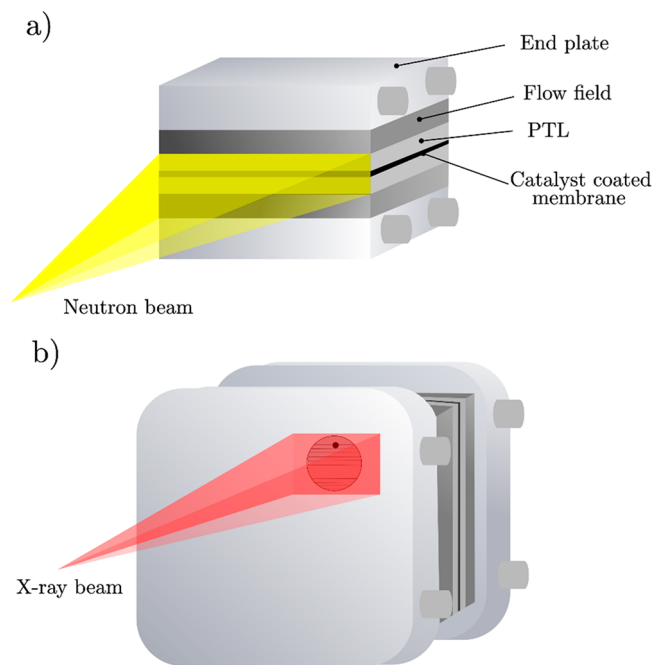


Figure 2. Schematic of the in operando imaging setups: (a) Neutron imaging setup, where the electrolyzer cell is oriented in an in-plane direction. The resulting images are used to calculate gas saturation in the commercial and PTP PTLs. (b) Subsecond X-ray synchrotron setup. The electrolyzer cell is oriented in the through-plane direction. Dynamic gas growth and snap-off from the PTL can be observed through the viewing region.

The neutron beam from the reactor core becomes attenuated as the beam penetrates the operating electrolyzer. We capture this change in attenuation to quantify the gas saturation of the PTL. The electrolyzer cell is mounted onto the stage to allow the neutron beams to traverse in the in-plane direction of the electrolyzer, thereby capturing the gas saturation profile in the through-plane direction of the PTL (i.e., thickness of the PTL). Once the neutron beam is attenuated by the electrolyzer, a scintillator ($\text{Gd}_2\text{O}_2\text{S:Tb}$) converts the transmitted neutrons to the visible light spectrum which are captured with an Andor Neo sCMOS detector. We achieve a spatial resolution of $15 \mu\text{m}$ with this setup, and a frame rate of 120 s per frame is selected to achieve sufficient neutron beam exposure. Two types of images are

acquired during in operando neutron imaging: the reference image and the operational image. The reference image is acquired when the PTL is fully saturated with liquid water, and operational images are acquired throughout the period during which the polarization curve is measured. At the reference state, there is an absence of applied current in the electrolyzer cell, and we flow liquid water for 30 min prior to the experiment to remove from the pores of the PTL. Operational images (i.e., images acquired at constant current, $i > 0$) are subsequently acquired.

Three image artifacts are corrected prior to quantifying the PTL gas saturation. First, we correct for the random noise arising from γ spots by the median combination of three subsequent images. Second, hot spots generated from the electronic components are corrected with a 3×3 pixel median filter. Finally, we apply an image registration process⁵⁶ to correct for image artifacts caused by the operating process of the NIST reactor.

The gas thickness in the PTL (amount of gas present in the PTL, t_{gas}) is quantified for each operating current density by applying a modified Beer–Lambert law⁵⁶ to the corrected neutron images

$$t_{\text{gas}} = \left(-\frac{\ln(I/I_0)}{\beta_w} + \frac{\sum_w^2}{4\beta_w^2} \right)^{1/2} - \frac{\sum_w}{2\beta_w} \quad (5)$$

where the gas thickness [mm] for each pixel is denoted as t_{gas} , and the pixel intensity of the operation and reference images are I and I_0 , respectively. We use the fitting parameters suggested by Hussey et al.,⁵⁶ where \sum_w and β_w are $[0.38483 \text{ mm}^{-1}]$ and $[-0.00947 \text{ mm}^{-2}]$, respectively. The volumetric fraction of gas (gas saturation, s_{gas}) in the PTL is further calculated for comparison by applying the following relation to the measured gas thickness

$$s_{\text{gas}} = \frac{t_{\text{gas}}}{L_{\text{PTL}} \cdot \varepsilon} \quad (6)$$

where L_{PTL} is the length of the PTL along the in-plane direction [mm], and ε is the porosity of the PTL. Porosities for the commercial and PTP PTLs are 35 % and 40 %, respectively.

Synchrotron X-ray Imaging for Visualizing Bubble Breakthrough. Subsecond synchrotron X-ray imaging is performed to investigate the dynamics of bubble breakthrough behavior (i.e., bubble growth and snap-off behavior on the PTL–flow field interface). In this experiment, we apply relatively low current densities ($i = 0.05 \text{ A/cm}^2$, 0.1 A/cm^2 , 0.25 A/cm^2 , and 0.5 A/cm^2) to minimize the formation of gas slugs in the channel at cell temperature of $40 \text{ }^\circ\text{C}$, since the aim is to elucidate the transport behavior of the PTPs in the PTL. Due to X-ray attenuation effects, separate custom hardware is used for the X-ray and neutron experiments. The flow fields are fabricated with graphite (rather than titanium), and the electrolyzer has an active area of $5 \text{ cm} \times 5 \text{ cm}$. We position the electrolyzer cell in the through-plane direction (i.e., membrane perpendicular to the beam axis) to visualize bubble dynamics at the PTL–flow field interface. A viewing region is machined into the end plates and the current collectors to minimize the X-ray penetration through the end plates. To observe the transient bubble dynamics at the through-pore, we machine a single through-pore in the PTL. The schematic of the setup is shown in Figure 2b.

The in operando X-ray synchrotron experiment is conducted at the Biomedical Imaging and Therapy Wiggler Insertion Device beamline located at the Canadian Light Source Inc. (Saskatoon, Canada⁵⁷). With an incident beam of 30 keV , we achieve a pixel resolution of $6.5 \text{ }\mu\text{m}$ at a temporal resolution of 0.15 s per frame using a complementary metal oxide semiconductor (CMOS) camera (C11440-22CU, Hamamatsu). The reference image is assumed to be acquired with the PTL fully saturated with liquid water in the absence of applied current. An in operando image is acquired over the last 2 min of each 10 min constant current measurement. The bubble dynamics are analyzed by normalizing the operation images with the reference image (I/I_0).

RESULTS AND DISCUSSION

Enhanced Electrochemical Performance with PTP PTL. Galvanostatic polarization curves and mass transport overpotentials are used to compare the electrochemical performance between the PTP PTL and commercial PTL as the anode PTL (Figure 3). We observe lower cell potentials for

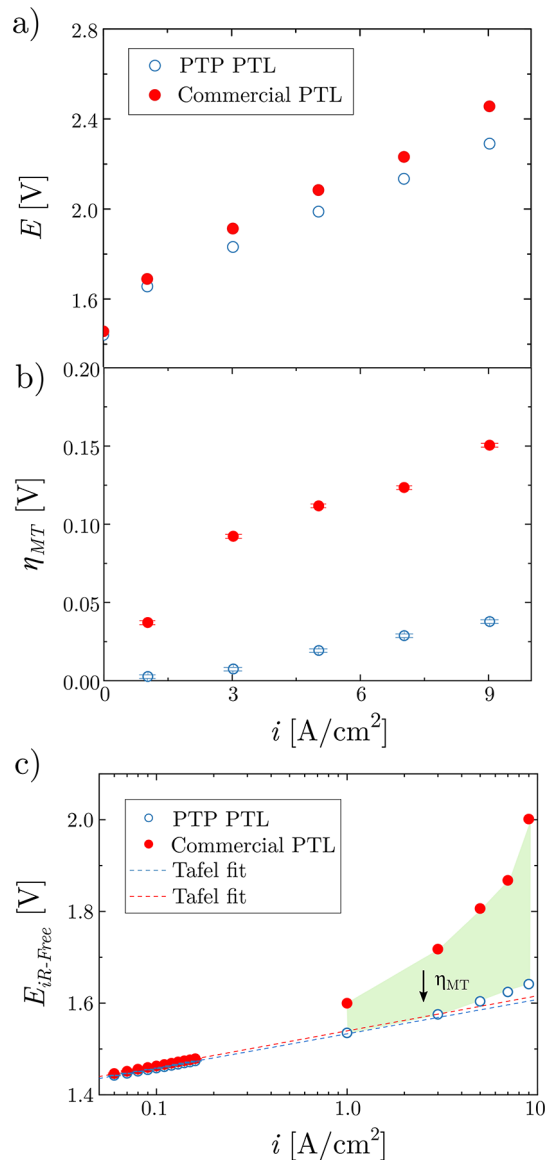


Figure 3. Comparing the electrochemical performance of the electrolyzers with the PTL with PTPs and the commercial PTL. (a) The polarization curves show that the PTL with PTPs exhibits superior performance compared to the commercial PTL over the tested current densities. (b) The mass transport overpotential (η_{MT}) calculated from the Tafel approximation shows a similar trend as (a). (c) The Tafel slope and iR -free cell potential for the PTP PTL and commercial PTL. The region in green indicates the reduction in mass transport overpotential due to the PTP PTL.

the cell assembly with the PTP PTL compared to the commercial PTL (PTP PTL exhibiting 166 mV lower at 9 A/cm^2 , Figure 3a). The cell assembly with the PTP PTL consistently outperforms up to a remarkably high current density ($i = 9 \text{ A/cm}^2$). A small inflection point is observed for the commercial PTL between 7 A/cm^2 and 9 A/cm^2 , which is

not seen for PTP PTL, suggesting that PTP PTL exhibits improved mass transport characteristics. Similarly, the mass transport overpotential (Figure 3b), calculated via the Tafel approximation, exhibits a comparable trend with the polarization curve. Specifically, the mass transport overpotential reduces more than 4-fold, from 150 mV ($i = 9 \text{ A/cm}^2$, commercial PTL) to 37 mV ($i = 9 \text{ A/cm}^2$, PTP PTL). The exchange current density measured from both PTLs exhibit comparable values ($i_{0,PTP} = 2.4 \times 10^{-5} \text{ A/cm}^2$ and $i_{0,commercial} = 2.5 \times 10^{-5} \text{ A/cm}^2$) which is in agreement to the values observed in the literature.²⁶ The electrolyzer with PTP PTL achieves a lower electrolyzer potential at the Tafel region, and this is attributed to the higher compression at the CL due to the smaller contact area of the PTP PTL. It is important to note that nonisothermal conditions are established at high current densities since the constant reactant flow rate of 1.5 mL/min was supplied to the cell, and we measure decreases in HFR with increasing current densities (due to improved ionic conductivity with increased temperature^{43,50}). However, the enhanced electrolyzer cell performance due to the presence of patterned through-pores has a dominant effect in this work.

By using the PTP PTL in the anode compartment, we reduce the contribution of the mass transport overpotential to the total cell overpotential by 12% at $i = 9 \text{ A/cm}^2$. When voltage efficiency is calculated using the relation⁵⁸

$$\eta_v = \frac{E_{TH}}{E_{cell}} \quad (7)$$

we show that the voltage efficiency of the electrolyzer cell improves by over 2% for all tested current densities and improves by 2.5% at 9 A/cm^2 . These efficiency increases are particularly significant considering that we did not modify any operating conditions of the electrolyzer cell.

We further elaborate the effect of the PTPs on mass transport by observing changes in potential with time during high current density operation. At $i = 9 \text{ A/cm}^2$, the commercial PTL experiences a sudden increase in cell potential, which we attribute to the mass transport limitation caused by the dynamics of generated gas at the reaction sites (Figure 4). Moreover, we also observe an improved gas removal mechanism from the PTP PTL, evidenced by the larger magnitude of potential fluctuations ($\pm 4 \text{ mV}$) (subfigure of Figure 4). The frequency in potential fluctuation is a direct

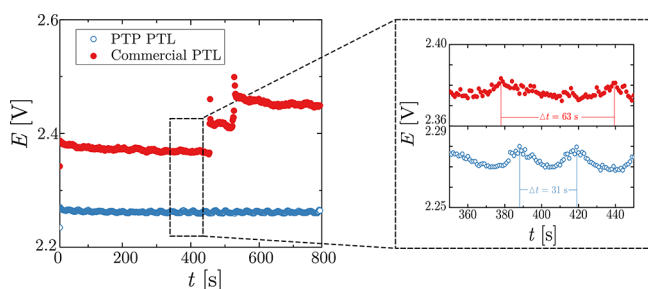


Figure 4. Transient potential response at 9 A/cm^2 for the PTP and commercial PTLs. The sudden increase in cell potential due to mass transport occurs at about 450 s for the commercial PTL. In the region indicated with a black dashed-box, we observe that the cell potential fluctuates for both PTLs. However, the potential for the PTP PTL fluctuates at a higher frequency, which indicates higher reactant uptake and gas removal rates through the PTPs.

indicator of gas accumulation and removal from the CL-PTL interface, since (1) we only observe the fluctuation in potential near the critical current density, and (2) the frequency is an order of magnitude lower than the frequency of the fluctuation in flow, possibly caused by the peristaltic pump (i.e., 7 s^{-1}). The higher frequency (i.e., 31 s^{-1}) confirms the effective gas removal characteristics of the PTP PTL relative to the commercial PTL (63 s^{-1}). Specifically, for the PTP PTL, the potential rapidly oscillates about a constant potential, demonstrating that the PTPs are facilitating rapid gas removal, despite the large gas generation rate accompanied by a high operating current density. The relatively slower gas removal mechanism of the commercial PTL leads to gas accumulation in the PTL; this manifests as a sharp increase in potential at $t = 470 \text{ s}$. Therefore, we demonstrate higher rates of gas removal and water delivery to the CL-PTL interface with our novel PTLs. Our work shows that our PTP PTL outperforms the commercial PTL, particularly at high current densities and near starvation conditions.

Effective Gas Removal through the Patterned Through-Pores. We further investigate the two-phase flow characteristics of the PTP PTL using in operando neutron imaging. In agreement with the literature,^{50,53,54} we observe minimal changes in PTL gas saturation with increasing current density (Figure 5). During our previous work,³⁰ we observed a

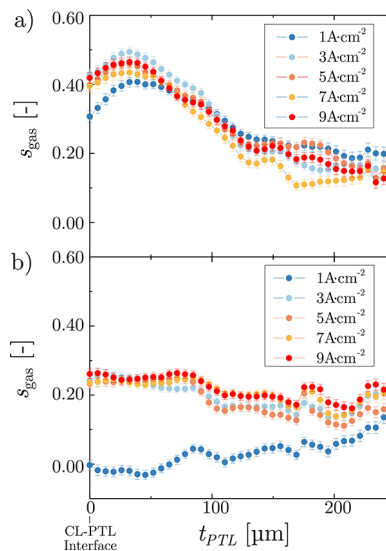


Figure 5. Gas saturation profiles for (a) the commercial PTL and (b) the PTP PTL. The thickness (t) refers to the through-plane position of the PTL, where $t = 0 \mu\text{m}$ indicates the position of the CL-PTL interface, and $t = 250 \mu\text{m}$ indicates the position of the CL-PTL interface. The gas saturation profile of the PTP PTL exhibits more homogeneity than the commercial PTL. The lower gas saturation in the PTP PTL at the CL-PTL interface is evidence of effective gas removal.

new performance indicator termed the *critical density* that refers to the performance inflection point where the PTL gas saturation increases sharply with increasing current density, thereby dominating the overpotentials of the electrolyzer; however, for the operating conditions in this work, we are operating below the critical current density. We observe that at the low current density (1 A/cm^2), the PTP PTL exhibits low gas saturation at the CL-PTL interface. We hypothesize that the low gas saturation at 1 A/cm^2 is related to less gas

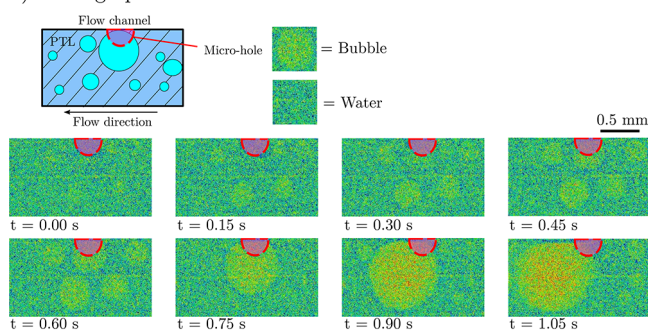
generation and the subsequent establishment of fewer gas transport pathways, which could be a characteristic of the PTP PTL. Further investigation is required to elucidate the underlying mechanism of the lower gas saturation for PTP PTLs. In this work, we focus on high current densities relevant to industrial PEM electrolyzers. At higher current densities, we observe distinct differences between the saturation profiles for the PTP PTL and commercial PTL (Figure 5). The overall gas saturation is significantly lower for the PTP PTL compared to the commercial PTL, whereby the PTP PTL has an 11 % lower average gas saturation in contrast to the commercial PTL, and this reduction in gas saturation is attributed to the enhanced mass transport behavior seen in Figure 3.

The PTP PTL exhibits a saturation profile favorable for reactant transport. The saturation profiles from the commercial PTL, shown in Figure 5a, exhibit similar profiles to those reported in the literature for conventional PTLs,^{50,53,59,60} where higher gas saturation is observed near the CL-PTL interface (Figure 5, $t = 0 \mu\text{m}$), while lower gas saturation is observed near the PTL-flow field interface (Figure 5, $t = 250 \mu\text{m}$). However, the saturation profile from the PTP PTL illustrates a flat profile, where the gas saturation near the CL-PTL interface is almost identical to the gas saturation near the PTL-flow field interface. The lower gas saturation adjacent to the CL-PTL interface as shown in Figure 5 reflects how generated gas preferentially percolates through the PTPs instead of branching out across the CL-PTL interface ($s_{\text{gas}} = 25.2\%$ for the PTP PTL and 44.8% for the commercial PTL for $i = 9 \text{ A/cm}^2$). Therefore, more reactant water near the CL-PTL interface is available for the oxygen evolution reaction with the PTP PTL. Our work highlights that the enhanced performance of the PTP PTL stems from lower gas saturations, particularly adjacent to the CL-PTL interface.

Improved Reactant Water Transport to Reaction Sites. Our results thus far demonstrate that the PTPs in the PTL exhibit lower cell potentials via effective gas removal at the CL-PTL interface. Here, we further elucidate the mechanism of enhanced gas removal via the PTPs, using in operando X-ray imaging of the growth of gas bubbles at the PTL-flow field interface. We hypothesize that the through-pores promote higher frequency gas snap-off at the PTL-flow field interface due to the favorable coalescence with neighboring bubbles in the flow channel. Upon coalescence, the gas clusters within the PTL pores (that are neighboring the through-pore) are subsequently removed by the water flowing in the channel, whereby upon gas removal, liquid water flows through the pathway, delivering reactant to the reaction sites.

The growth and detachment behaviors of gas bubbles at the PTL-flow field interface are imaged as shown in Figure 6 to investigate the enhancement of mass transport in the PTP PTL. We observe a higher volume of gas flow in the through-pore compared to the regular pores in the PTL. The bubble growth from the through-pore occurs over a period of $\sim 0.3 \text{ s}$ ($t = 0.30 \text{ s}$ to 0.60 s , in Figure 6a), which is noticeably shorter than the bubble growth period from regular pores in the commercial PTL transpiring over $t > 2.88 \text{ s}$ (Figure 6b). In addition, the bubble snap-off duration from the through-pore is approximately $t = 1.05 \text{ s}$ while the bubble snap-off duration of the commercial PTL is $t = 11 \text{ s}$. This shows that through-pores contribute significantly in reducing gas snap-off times via higher gas removal rates. The lower gas saturation of the PTP PTL observed via neutron imaging is attributed to this faster gas removal rate.

a) Through-pore PTL



b) Commercial PTL

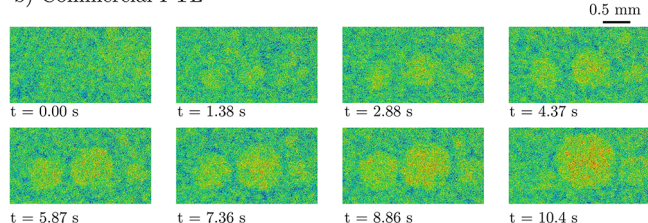


Figure 6. Bubble growth in the channel from the (a) through-pore PTL and (b) commercial PTL. The bubble growth initiates from the through-pore at $t = 0.30 \text{ s}$, and at $t = 0.75 \text{ s}$, the through-pore bubble coalesces with neighboring bubbles. We observe the emergence of a neighboring bubble after this coalescence at $t = 0.90 \text{ s}$, and this new bubble is flushed away as the through-pore bubble is snapped off ($t > 1.05 \text{ s}$). Since each snap off activity leads to water intake at the reaction site, through-pores lead to higher frequencies of reactant water intake at the reaction sites. The time required for bubble snap-off is substantially longer for the commercial PTL ($t > 10.4 \text{ s}$).

We observe an additional interesting transient behavior that promotes enhanced mass transport in the PTP PTL. The gas bubble from the through-pore continues to grow until the bubble coalesces with its neighboring bubbles (observed in Figure 6a at $t = 0.75 \text{ s}$). Gas permeation pathways in the PTL are immediately filled with water following bubble coalescence, and we hypothesize that this is a crucial mode of reactant transport under mass transport dominated conditions. We further observe the growth of a new neighboring bubble post coalescence (Figure 6a, $t = 0.90 \text{ s}$), which subsequently coalesces with the bubble snapped-off from the PTP ($t = 1.05 \text{ s}$). The snap-off diameters for the PTP PTL and commercial PTL are 1 mm (equal to the channel width) and 0.8 mm , respectively. Additionally, this snapped-off bubble traversing through the channel further coalesces with other residing bubbles in its pathway, enhancing mass transport not only near the through-pore but throughout the entire cell. Hence, the through-pore leads to more frequent coalescence and emergence of new bubbles consequently increasing the frequency of water transport to the reaction sites. Yet, since the bubbles grow and exit from the commercial PTL at much slower rates, the coalescence and subsequent replenishment of water to the reaction sites are also delayed substantially, resulting in significant mass transport losses at high current densities.

Our results demonstrate the advantages of the PTP structure for enhanced two-phase transport within the PTL and the subsequent improvement in electrochemical performance. We present a highly promising opportunity for achieving higher current density performance with PEM electrolyzers.

CONCLUSION

Gas evolving electrochemical energy conversion must adopt novel materials to transform efficiencies and cost for commercial viability. In this work, we present novel patterned PTL materials and explain the microscale multiphase transport behavior that underpins the enhanced mass transport behavior in PEM electrolyzers. By designing patterned through-pores in a commercial PTL, the mass transport overpotential of an electrolyzer cell is reduced 4-fold in comparison to the commercial PTL at high current density operation ($i = 9 \text{ A/cm}^2$). We employ in operando neutron imaging to quantify the steady state gas saturation inside the PTL, and we perform subsecond X-ray synchrotron imaging to visualize the dynamic two-phase flow behavior at the PTL-flow field interface to illustrate the improvement in the mass transport behavior when using the PTP PTL. Through in operando neutron imaging, we observe that gas saturation near the CL-PTL interface is reduced by 43.5 % with the application of the PTP PTL. Moreover, using subsecond X-ray synchrotron imaging, we show an improved water uptake mechanisms in the PTP PTL. Specifically, the faster bubble growth at the through-pore and the subsequent snap-off leads to more frequent liquid water uptake rates at the reaction sites, which significantly reduces undesired mass transport losses. By simply adding patterned through-pores to a commercial PTL, we improve reactant transport mechanisms and significantly reduce mass transport losses by 76.7 % at a high current density of 9 A/cm^2 . Our finding is highly valuable for achieving high current density operations in PEM electrolyzers and more generally for gas evolving electrochemical energy conversion technologies that are also hindered by inefficient multiphase transport dynamics.

AUTHOR INFORMATION

Corresponding Author

Aimy Bazylak – *Thermofluids for Energy and Advanced Material Laboratory, Department of Mechanical and Industrial Engineering, Institute for Sustainable Energy, Faculty of Applied Science and Engineering, University of Toronto, Toronto, ON M5S 3G8, Canada;* orcid.org/0000-0002-9594-4930;
Email: abazylak@mie.utoronto.ca

Authors

Jason K. Lee – *Thermofluids for Energy and Advanced Material Laboratory, Department of Mechanical and Industrial Engineering, Institute for Sustainable Energy, Faculty of Applied Science and Engineering, University of Toronto, Toronto, ON M5S 3G8, Canada*

ChungHyuk Lee – *Thermofluids for Energy and Advanced Material Laboratory, Department of Mechanical and Industrial Engineering, Institute for Sustainable Energy, Faculty of Applied Science and Engineering, University of Toronto, Toronto, ON M5S 3G8, Canada*

Kieran F. Fahy – *Thermofluids for Energy and Advanced Material Laboratory, Department of Mechanical and Industrial Engineering, Institute for Sustainable Energy, Faculty of Applied Science and Engineering, University of Toronto, Toronto, ON M5S 3G8, Canada*

Pascal J. Kim – *Thermofluids for Energy and Advanced Material Laboratory, Department of Mechanical and Industrial Engineering, Institute for Sustainable Energy, Faculty of Applied Science and Engineering, University of Toronto, Toronto, ON M5S 3G8, Canada*

Kevin Krause – *Thermofluids for Energy and Advanced Material Laboratory, Department of Mechanical and Industrial Engineering, Institute for Sustainable Energy, Faculty of Applied Science and Engineering, University of Toronto, Toronto, ON M5S 3G8, Canada*

Jacob M. LaManna – *Physical Measurement Laboratory, National Institute of Standards and Technology, Gaithersburg, Maryland 20874, United States*

Elias Baltic – *Physical Measurement Laboratory, National Institute of Standards and Technology, Gaithersburg, Maryland 20874, United States*

David L. Jacobson – *Physical Measurement Laboratory, National Institute of Standards and Technology, Gaithersburg, Maryland 20874, United States*

Daniel S. Hussey – *Physical Measurement Laboratory, National Institute of Standards and Technology, Gaithersburg, Maryland 20874, United States;* orcid.org/0000-0002-2851-4367

Complete contact information is available at:

<https://pubs.acs.org/10.1021/acsaem.0c01239>

Notes

¹Certain trade names and company products are mentioned in the text or identified in an illustration in order to adequately specify the experimental procedure and equipment used. In no case does such identification imply recommendation or endorsement by the National Institute of Standards and Technology, nor does it imply that the products are necessarily the best available for the purpose.

The authors declare no competing financial interest.

ACKNOWLEDGMENTS

This work was supported by the Natural Sciences and Engineering Research Council of Canada (NSERC) Discovery Grants Program and the Canada Research Chairs Program. Graduate scholarships awarded to Jason Keonhag Lee from NSERC Alexander Graham Bell Canada Graduate Scholarships – Doctoral Program, Queen Elizabeth II/Edward Rygiel Graduate Scholarship in Science and Technology, Ontario Graduate Scholarship and Glynn Williams Fellowships are also gratefully acknowledged. The graduate scholarship to Kevin Krause from the Mrs. Vijayalakshmi Graduate Scholarship in Sustainable Energy is gratefully acknowledged. A portion of this work was supported by the National Institute of Standards and Technology and the NIST Physical Measurement Laboratory. Research described in this paper was performed at the BMIT facility at the Canadian Light Source, which is supported by the Canada Foundation for Innovation, Natural Sciences and Engineering Research Council of Canada, the University of Saskatchewan, the Government of Saskatchewan, Western Economic Diversification Canada, the National Research Council Canada, and the Canadian Institutes of Health Research. Authors acknowledge generous support from the CLS Post-Doctoral and Graduate Student Travel Support Program. The authors would also like to acknowledge Denise Miller, Sergey Gasilov, Ning Zhu, Adam Webb, and the entire BMIT group of the Canadian Light Source for their generous assistance.

REFERENCES

- (1) Ursua, A.; Gandia, L. M.; Sanchis, P. Hydrogen Production From Water Electrolysis: Current Status and Future Trends. *Proc. IEEE* **2012**, *100*, 410–426.

- (2) Carmo, M.; Fritz, D. L.; Mergel, J.; Stolten, D. A comprehensive review on PEM water electrolysis. *Int. J. Hydrogen Energy* **2013**, *38*, 4901–4934.
- (3) Bessarabov, D.; Wang, H.; Li, H.; Zhao, N. In *PEM electrolysis for hydrogen production: principles and applications*; CRC press: 2016.
- (4) Babic, U.; Suermann, M.; Büchi, F. N.; Gubler, L.; Schmidt, T. J. Critical Review—Identifying Critical Gaps for Polymer Electrolyte Water Electrolysis Development. *J. Electrochem. Soc.* **2017**, *164*, F387–F399.
- (5) Grigoriev, S.; Fateev, V.; Bessarabov, D.; Millet, P. Current status, research trends, and challenges in water electrolysis science and technology. *Int. J. Hydrogen Energy* **2020**, 109.
- (6) Schmidt, O.; Gambhir, A.; Staffell, I.; Hawkes, A.; Nelson, J.; Few, S. Future cost and performance of water electrolysis: An expert elicitation study. *Int. J. Hydrogen Energy* **2017**, *42*, 30470–30492.
- (7) Müller, M.; Carmo, M.; Glösen, A.; Hehemann, M.; Saba, S.; Zwaygardt, W.; Stolten, D. Water management in membrane electrolysis and options for advanced plants. *Int. J. Hydrogen Energy* **2019**, *44*, 10147–10155.
- (8) Gago, A. S.; Ansar, S. A.; Saruhan, B.; Schulz, U.; Lettenmeier, P.; Cañas, N. A.; Gazdzicki, P.; Morawietz, T.; Hiesgen, R.; Arnold, J.; Friedrich, K. A. Protective coatings on stainless steel bipolar plates for proton exchange membrane (PEM) electrolyzers. *J. Power Sources* **2016**, *307*, 815–825.
- (9) Shirvanian, P.; van Berkel, F. Novel Components in Proton Exchange Membrane Water Electrolyzers (PEMWE): Status, Challenges and Future Needs. *Electrochem. Commun.* **2020**, *114*, 106704.
- (10) Villagra, A.; Millet, P. An analysis of PEM water electrolysis cells operating at elevated current densities. *Int. J. Hydrogen Energy* **2019**, *44*, 9708–9717.
- (11) Amano, F.; Furusho, Y.; Hwang, Y. Amorphous Iridium and Tantalum Oxides Layer Coated on Titanium Felt for Electrocatalytic Oxygen Evolution Reaction. *ACS Applied Energy Materials* **2020**, *3*, 4531.
- (12) Mo, J.; Stefanov, B. I.; Lau, T. H.; Chen, T.; Wu, S.; Wang, Z.; Gong, X.; Wilkinson, I.; Schmid, G.; Tsang, S. C. E. Superior Performance of Ag over Pt for Hydrogen Evolution Reaction in Water Electrolysis under High Overpotentials. *ACS Applied Energy Materials* **2019**, *2*, 1221–1228.
- (13) Li, Q.; Li, J.; Xu, J.; Zhang, N.; Li, Y.; Liu, L.; Pan, D.; Wang, Z.; Deepak, F. L. Ultrafine-Grained Porous Ir-Based Catalysts for High-Performance Overall Water Splitting in Acidic Media. *ACS Applied Energy Materials* **2020**, *3*, 3736–3744.
- (14) Hyun, J.; Doo, G.; Yuk, S.; Lee, D.; Lee, D. W.; Choi, S.; Kwen, J.; Kang, H.; Tenne, R.; Lee, S. G. Magnetic field-induced through-plane alignment of the proton highway in a proton exchange membrane. *ACS Applied Energy Materials* **2020**, *3*, 4619.
- (15) Suermann, M.; Schmidt, T. J.; Büchi, F. N. Investigation of Mass Transport Losses in Polymer Electrolyte Electrolysis Cells. *ECS Trans.* **2015**, *69*, 1141–1148.
- (16) Dedigama, I.; Angeli, P.; Ayers, K.; Robinson, J. B.; Shearing, P. R.; Tsaoulidis, D.; Brett, D. J. In situ diagnostic techniques for characterisation of polymer electrolyte membrane water electrolyzers - Flow visualisation and electrochemical impedance spectroscopy. *Int. J. Hydrogen Energy* **2014**, *39*, 4468–4482.
- (17) Lettenmeier, P.; Kolb, S.; Zielke, L.; Thiele, S.; Fallisch, A.; Sata, N.; Gago, A. S.; Friedrich, K. A. Comprehensive Investigation of Novel Pore-Graded Gas Diffusion Layers for High-Performance and Cost-Effective Proton Exchange Membrane Electrolyzers. *Energy Environ. Sci.* **2017**, *10*, 2521.
- (18) Majasan, J. O.; Iacoviello, F.; Shearing, P. R.; Brett, D. J. Effect of Microstructure of Porous Transport Layer on Performance in Polymer Electrolyte Membrane Water Electrolyser. *Energy Procedia* **2018**, *151*, 111–119.
- (19) Siracusano, S.; Trocino, S.; Briguglio, N.; Baglio, V.; Aricò, A. S. Electrochemical impedance spectroscopy as a diagnostic tool in polymer electrolyte membrane electrolysis. *Materials* **2018**, *11*, 1368.
- (20) Siracusano, S.; Trocino, S.; Briguglio, N.; Pantò, F.; Aricò, A. S. Analysis of performance degradation during steady-state and load-thermal cycles of proton exchange membrane water electrolysis cells. *J. Power Sources* **2020**, *468*, 228390.
- (21) Garcia-Navarro, J.; Schulze, M.; Friedrich, K. Measuring and modeling mass transport losses in proton exchange membrane water electrolyzers using electrochemical impedance spectroscopy. *J. Power Sources* **2019**, *431*, 189–204.
- (22) Lickert, T.; Kiermaier, M. L.; Bromberger, K.; Ghinaiya, J.; Metz, S.; Fallisch, A.; Smolinka, T. On the influence of the anodic porous transport layer on PEM electrolysis performance at high current densities. *Int. J. Hydrogen Energy* **2020**, *45*, 6047–6058.
- (23) Parra-Restrepo, J.; Bligny, R.; Dillet, J.; Didierjean, S.; Stemmelen, D.; Moyne, C.; Degiovanni, A.; Maranzana, G. Influence of the porous transport layer properties on the mass and charge transfer in a segmented PEM electrolyzer. *Int. J. Hydrogen Energy* **2020**, *45*, 8094–8106.
- (24) Babic, U.; Schmidt, T. J.; Gubler, L. Communication—Contribution of Catalyst Layer Proton Transport Resistance to Voltage Loss in Polymer Electrolyte Water Electrolyzers. *J. Electrochem. Soc.* **2018**, *165*, J3016–J3018.
- (25) Lopata, J.; Kang, Z.; Young, J.; Bender, G.; Weidner, J.; Shimpalee, S. Effects of the Transport/Catalyst Layer Interface and Catalyst Loading on Mass and Charge Transport Phenomena in Polymer Electrolyte Membrane Water Electrolysis Devices. *J. Electrochem. Soc.* **2020**, *167*, 064507.
- (26) Ito, H.; Maeda, T.; Nakano, A.; Hwang, C. M.; Ishida, M.; Kato, A.; Yoshida, T. Experimental study on porous current collectors of PEM electrolyzers. *Int. J. Hydrogen Energy* **2012**, *37*, 7418–7428.
- (27) Suermann, M.; Takanohashi, K.; Lamibrac, A.; Schmidt, T. J.; Büchi, F. N. Influence of operating conditions and material properties on the mass transport losses of polymer electrolyte water electrolysis. *J. Electrochem. Soc.* **2017**, *164*, F973–F980.
- (28) Schuler, T.; Schmidt, T. J.; Büchi, F. N. Polymer Electrolyte Water Electrolysis: Correlating Performance and Porous Transport Layer Structure: Part II. Electrochemical Performance Analysis. *J. Electrochem. Soc.* **2019**, *166*, F555–F565.
- (29) Schuler, T.; Kimura, T.; Schmidt, T. J.; Büchi, F. N. Towards a generic understanding of oxygen evolution reaction kinetics in polymer electrolyte water electrolysis. *Energy Environ. Sci.* **2020**, *13*, 2153.
- (30) Grigoriev, S. A.; Millet, P.; Volobuev, S. A.; Fateev, V. N. Optimization of porous current collectors for PEM water electrolyzers. *Int. J. Hydrogen Energy* **2009**, *34*, 4968–4973.
- (31) Lettenmeier, P.; Kolb, S.; Burggraf, F.; Gago, A. S.; Friedrich, K. A. Towards developing a backing layer for proton exchange membrane electrolyzers. *J. Power Sources* **2016**, *311*, 153–158.
- (32) Lettenmeier, P.; Wang, R.; Aboutallah, R.; Helmly, S.; Morawietz, T.; Hiesgen, R.; Kolb, S.; Burggraf, F.; Kallo, J.; Gago, A. S.; Friedrich, K. A. Durable Membrane Electrode Assemblies for Proton Exchange Membrane Electrolyzer Systems Operating at High Current Densities. *Electrochim. Acta* **2016**, *210*, 502–511.
- (33) Kang, Z.; Yu, S.; Yang, G.; Li, Y.; Bender, G.; Pivovar, B. S.; Green, J. B.; Zhang, F. Performance improvement of proton exchange membrane electrolyzer cells by introducing in-plane transport enhancement layers. *Electrochim. Acta* **2019**, *316*, 43–51.
- (34) Kang, Z.; Mo, J.; Yang, G.; Retterer, S. T.; Cullen, D. A.; Toops, T. J.; Green, J. B., Jr; Mench, M. M.; Zhang, F. Investigation of thin/well-tunable liquid/gas diffusion layers exhibiting superior multifunctional performance in low-temperature electrolytic water splitting. *Energy Environ. Sci.* **2017**, *10*, 166–175.
- (35) Schuler, T.; Ciccone, J. M.; Krentscher, B.; Marone, F.; Peter, C.; Schmidt, T. J.; Büchi, F. N. Hierarchically Structured Porous Transport Layers for Polymer Electrolyte Water Electrolysis. *Adv. Energy Mater.* **2020**, *10*, 2070009.
- (36) Ito, H.; Maeda, T.; Nakano, A.; Hwang, C. M.; Ishida, M.; Kato, A.; Yoshida, T. Effect of titanium powder loading in microporous layer on a polymer electrolyte unitized reversible fuel cell. *ECS Trans.* **2011**, *41*, 469–477.

- (37) Lee, C.; Zhao, B.; Aboutallah, R.; Wang, R.; Bazylak, A. Compressible-Gas Invasion into Liquid-Saturated Porous Media: Application to Polymer-Electrolyte-Membrane Electrolyzers. *Phys. Rev. Appl.* **2019**, *11*, 054029.
- (38) Lee, J.; Bazylak, A. Stochastic Modelling For Controlling the Structure of Sintered Titanium Powder-Based Porous Transport Layers for Polymer Electrolyte Membrane Electrolyzers. *J. Electrochem. Soc.* **2019**, *166*, F1000–F1006.
- (39) Kim, P. J.; Lee, C.; Lee, J. K.; Fahy, K. F.; Bazylak, A. In-plane Mass Transport in Polymer Electrolyte Membrane Electrolyzer Porous Transport Layers with Through Pores. *ECS Trans.* **2019**, *92*, 787.
- (40) Kim, P. J.; Lee, C. H.; Lee, J. K.; Fahy, K.; Bazylak, A. In-plane transport in water electrolyzer porous transport layers with through pores. *J. Electrochem. Soc.* **2020**, *167*, 124522.
- (41) Dedigama, I.; Angeli, P.; van Dijk, N.; Millichamp, J.; Tsaoulidis, D.; Shearing, P. R.; Brett, D. J. Current density mapping and optical flow visualisation of a polymer electrolyte membrane water electrolyser. *J. Power Sources* **2014**, *265*, 97–103.
- (42) Ito, H.; Maeda, T.; Nakano, A.; Hasegawa, Y.; Yokoi, N.; Hwang, C.; Ishida, M.; Kato, A.; Yoshida, T. Effect of flow regime of circulating water on a proton exchange membrane electrolyzer. *Int. J. Hydrogen Energy* **2010**, *35*, 9550–9560.
- (43) Lee, C.; Lee, J. K.; George, M. G.; Fahy, K. F.; LaManna, J. M.; Baltic, E.; Hussey, D. S.; Jacobson, D. L.; Bazylak, A. Reconciling temperature-dependent factors affecting mass transport losses in polymer electrolyte membrane electrolyzers. *Energy Convers. Manage.* **2020**, *213*, 112797.
- (44) Majasan, J. O.; Cho, J. I.; Maier, M.; Dedigama, I.; Shearing, P. R.; Brett, D. J. Effect of Anode Flow Channel Depth on the Performance of Polymer Electrolyte Membrane Water Electrolyser. *ECS Trans.* **2018**, *85*, 1593–1603.
- (45) Selamet, O. F.; Becerikli, F.; Mat, M. D.; Kaplan, Y. Development and testing of a highly efficient proton exchange membrane (PEM) electrolyzer stack. *Int. J. Hydrogen Energy* **2011**, *36*, 11480–11487.
- (46) Siracusano, S.; Baglio, V.; Di Blasi, A.; Briguglio, N.; Stassi, A.; Ornelas, R.; Trifoni, E.; Antonucci, V.; Arico, A. Electrochemical characterization of single cell and short stack PEM electrolyzers based on a nanosized IrO₂ anode electrocatalyst. *Int. J. Hydrogen Energy* **2010**, *35*, 5558–5568.
- (47) Ojong, E. T.; Kwan, J. T. H.; Nouri-Khorasani, A.; Bonakdarpour, A.; Wilkinson, D. P.; Smolinka, T. Development of an experimentally validated semi-empirical fully-coupled performance model of a PEM electrolysis cell with a 3-D structured porous transport layer. *Int. J. Hydrogen Energy* **2017**, *42*, 25831.
- (48) Hoeh, M. In *In-Operando Synchrotron X-Ray and Neutron Radiography Studies of Polymer Electrolyte Membrane Water Electrolyzers*; 228th ECS Meeting (October 11–15, 2015); ECS: 2015.
- (49) Leonard, E.; Shum, A. D.; Normile, S.; Sabarirajan, D. C.; Yared, D. G.; Xiao, X.; Zenyuk, I. V. Operando X-ray tomography and sub-second radiography for characterizing transport in polymer electrolyte membrane electrolyzer. *Electrochim. Acta* **2018**, *276*, 424–433.
- (50) Lee, C.; Lee, J.; Zhao, B.; Fahy, K.; LaManna, J.; Baltic, E.; Hussey, D.; Jacobson, D.; Schulz, V.; Bazylak, A. Temperature-dependent gas accumulation in polymer electrolyte membrane electrolyzer porous transport layers. *J. Power Sources* **2020**, *446*, 227312.
- (51) Lee, C.; Banerjee, R.; Ge, N.; Lee, J. K.; Zhao, B.; Baltic, E.; LaManna, J. M.; Hussey, D. S.; Jacobson, D. L.; Aboutallah, R.; Wang, R.; Bazylak, A. The effect of cathode nitrogen purging on cell performance and in operando neutron imaging of a polymer electrolyte membrane electrolyzer. *Electrochim. Acta* **2018**, *279*, 91.
- (52) Panchenko, O.; Borgardt, E.; Zwaygardt, W.; Hackemüller, F. J.; Bram, M.; Kardjilov, N.; Arlt, T.; Manke, I.; Müller, M.; Stolten, D.; Lehnert, W. In-situ two-phase flow investigation of different porous transport layer for a polymer electrolyte membrane (PEM) electrolyzer with neutron spectroscopy. *J. Power Sources* **2018**, *390*, 108–115.
- (53) Seweryn, J.; Biesdorf, J.; Schmidt, T. J.; Boillat, P. Communication—Neutron Radiography of the Water/Gas Distribution in the Porous Layers of an Operating Electrolyser. *J. Electrochem. Soc.* **2016**, *163*, F3009–F3011.
- (54) Lee, J. K.; Lee, C.; Fahy, K. F.; Zhao, B.; LaManna, J. M.; Baltic, E.; Jacobson, D. L.; Hussey, D. S.; Bazylak, A. Critical Current Density as a Performance Indicator for Gas-Evolving Electrochemical Devices. *Cell Reports Physical Science* **2020**, *1*, 100147.
- (55) LeRoy, R. L.; Bowen, C. T.; LeRoy, D. J. The thermodynamics of aqueous water electrolysis. *J. Electrochem. Soc.* **1980**, *127*, 1954–1962.
- (56) Hussey, D. S.; Spornjak, D.; Weber, A. Z.; Mukundan, R.; Fairweather, J.; Brosha, E. L.; Davey, J.; Spindelov, J. S.; Jacobson, D. L.; Borup, R. L. Accurate measurement of the through-plane water content of proton-exchange membranes using neutron radiography. *J. Appl. Phys.* **2012**, *112*, 104906.
- (57) Wysokinski, T. W.; Chapman, D.; Adams, G.; Renier, M.; Suortti, P.; Thomlinson, W. Beamlines of the biomedical imaging and therapy facility at the Canadian light source - Part I. *Nucl. Instrum. Methods Phys. Res., Sect. A* **2007**, *582*, 73–76.
- (58) Kumar, S. S.; Himabindu, V. Hydrogen production by PEM water electrolysis—A review. *Materials Science for Energy Technologies* **2019**, *2*, 442–454.
- (59) Lee, C.; Lee, J.; Zhao, B.; Fahy, K.; Bazylak, A. Transient Gas Distribution in Porous Transport Layers of Polymer Electrolyte Membrane Electrolyzers. *J. Electrochem. Soc.* **2020**, *167*, 024508.
- (60) Lee, J.; Lee, C.; Bazylak, A. Pore network modelling to enhance liquid water transport through porous transport layers for polymer electrolyte membrane electrolyzers. *J. Power Sources* **2019**, *437*, 226910.